

Assessing Nickel Titanium Binary Systems Using Structural Search Methods and Ab Initio Calculations

Logan Lang,* Adam Payne,* Irais Valencia-Jaime,* Matthieu J. Verstraete,* Alejandro Bautista-Hernández,* and Aldo H. Romero*

Cite This: <https://dx.doi.org/10.1021/acs.jpcc.0c10453>

Read Online

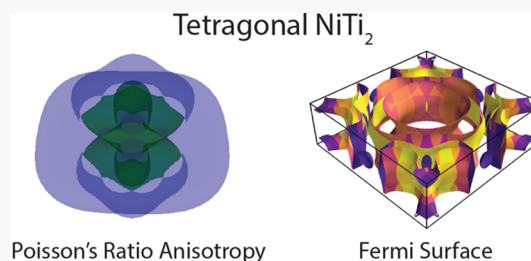
ACCESS |

Metrics & More

Article Recommendations

Supporting Information

ABSTRACT: Nickel titanium, also known as nitinol, is a prototypical shape memory alloy, a property intimately linked to a phase transition in the microstructure, which allows the meso/macroscale sample shape to be recovered after thermal cycling. Not much is known about the other alloys in this binary system, which prompted our computational investigation of other compositions. In this work, structures are found by probing the potential energy surfaces of NiTi binary systems using a minima hopping method, in combination with ab initio electronic structure calculations. We find stable structures in 34 different stoichiometries and calculate derived physical properties of the low energy phases. From the results of this analysis a new convex hull is formed that is lower in energy than those in the Materials Project and Open Quantum Materials Databases. Two previously unreported phases are discovered for the NiTi₂ and Ni₅Ti compositions, and two metastable states in NiTi and NiTi₂ shows signs of negative linear compression and negative Poisson ratio, respectively.



INTRODUCTION

Nitinol is a nickel/titanium alloy in nearly equiatomic (50–51% Ni) ratios, which is well-known to display both superelasticity and shape memory.^{1–3} This material has many applications in thermal actuators, which replace more traditional solenoids, damping systems in structural engineering applications, such as intelligently reinforced concrete for bridges and buildings, and a wide variety of biomedical applications, thanks to its good biocompatibility.^{4–8} Despite its wide use, NiTi still presents some engineering challenges, such as dramatic fatigue failure after just a few thermal cycles and a strong variability in the measured transition temperatures. The strain-controlled performance of NiTi is superior to many other metals, but in structural engineering applications it is subject to massive strains which induce fatigue failure. Very little is known outside of the equiatomic composition: fully exploring the various stable and metastable phases of NiTi will enable a better understanding of its properties and inform attempts to further improve its performance.

METHODS

Density Functional Theory. All relaxations, both ionic and electric, were performed using density functional theory (DFT) as implemented in the Vienna Ab-Initio Simulation Package (VASP).^{9,10} The projector augmentation wave (PAW)^{11,12} method was used to describe the electrons of our systems. For Ni, 16 valence electrons were used and for Ti 10. The generalized gradient approximation (GGA) as parametrized by Perdew, Burke, and Ernzerhof (PBE) was used for the exchange-

correlation functional.¹³ A Monkhorst–Pack k-mesh was used to sample the Brillouin zone,¹⁴ with a density adapted to the unit cell and dispersion. For hexagonal structures, a γ -centered mesh was used to correctly capture symmetry. The k-mesh was optimized to ensure total energy differences between consecutive mesh sizes to less than 10⁻⁶ eV, and all forces were converged to better than 10⁻³ eV/Å. Electronic energies were converged to within 10⁻⁵ eV in the self-consistent cycle, and strain was converged to less than 10⁻³ kBar. All DFT calculations were performed at zero pressure and temperature. In order to determine if any phases were magnetic, spin-polarized calculations were performed for structures within 50 meV of the convex hull. The results revealed there were no magnetic moments for any of the phases.

Thermal and mechanical stability and derived properties were assessed by determining elastic constants through the use of lattice distortions (six finite deformations for each lattice) to derive the stress–strain relationship and construct the elastic tensor, as implemented in the VASP code.¹⁵ The elastic constants are converged to a tolerance of 1 kBar. The mechanical stability was assessed through mechanical properties, such as the Bulk, Young, and Shear moduli, as well as the Poisson ratio.

Received: November 20, 2020

Revised: December 19, 2020

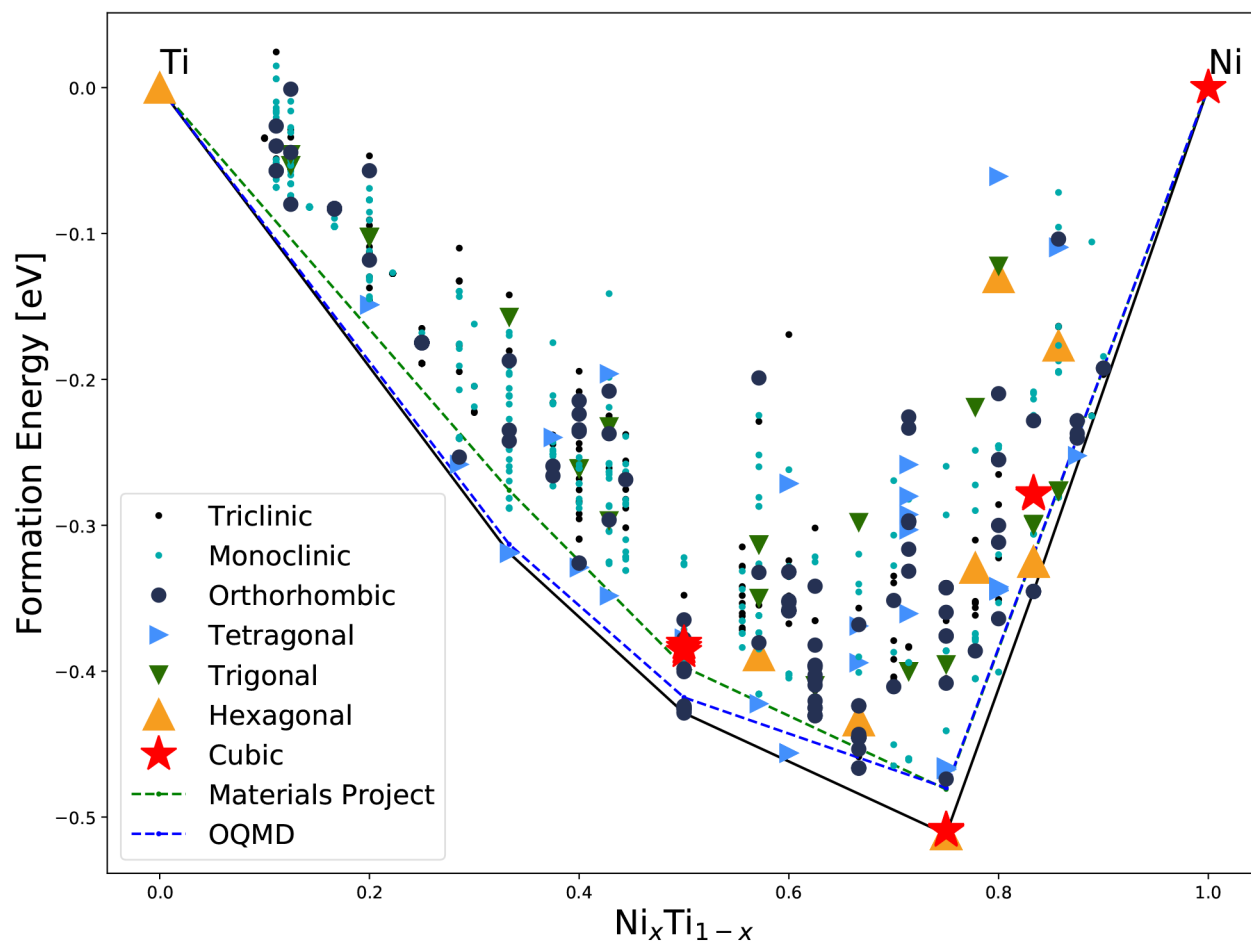


Figure 1. Convex hull for NiTi. Since cubic structures are necessary for the shape-memory effect, the convex hull points are decorated to determine if a relationship exists between cubic phases and composition. Low energy structures obtained from OQMD and MP databases are reoptimized with the same numerical tolerances as our results.

Their angular dependence was determined using the ELATE open-source software package.¹⁶ Band structure plotting and Fermi surface analysis was performed using the PyProcar software package.¹⁷ The frozen-phonon method, as implemented in the PHONOPY package,¹⁸ was used to assess dynamical stability. The forces were fitted from the interatomic force constants generated by the finite differences method in PHONOPY. Phonon calculations were performed by constructing $2 \times 2 \times 2$ supercells to generate phonon spectra.

Structural prediction uses a variety of methods to effectively explore a material's potential energy surface. The surface is a multidimensional representation of all possible crystal phases of a compound, given by the free energy of the different configurations as a function of the crystal degrees of freedom. In the case of crystal structure search, these are the ionic coordinates and unit cell lattice vectors. This implies a potential energy surface (PES) has dimensions of $3N + 6$ for a system with N atoms. Energetically stable configurations of ions will correspond to minima on this surface, so the problem of structural prediction is equivalent to locating the minima, both local and global, of the PES. This is a formidable task in general, and there are a number of different global search methods which have been used for structural search. Some of the more popular methods are genetic algorithms,¹⁹ meta-heuristic methods such as the particle swarm,²⁰ the firefly algorithm,²¹ simulated annealing,²² and basin hopping.²³

Minima Hopping Method. Here, we use the minima hopping method (MHM)^{24,25} to locate the low-energy phases of binary NiTi. This methodology has been proven to be able to describe the convex hull of many different materials.^{26,27} We use short density functional theory based molecular dynamics (MD) simulations to effectively hop between basins on the PES. The searcher begins with a single point on the PES, which corresponds to some configuration of atoms in a box. This point will reside within the basin of attraction of a local minimum of the PES, and geometric relaxation is performed with DFT to reach this local minimum. To escape the minimum, the initial velocities of the next MD simulation are aligned along the softest-mode direction found from the local environment. Following the Bell–Evans–Polanyi principle,²⁸ this forces the searcher into a new basin of attraction, where the process then repeats. In addition, a feedback mechanism is implemented to avoid revisiting previously located minima.

In this work, the MHM is used to map out the PES of $\text{Ni}_x\text{Ti}_{1-x}$ ($0 < x < 1$) with up to 10 atoms per cell. Within this constraint, 34 different stoichiometries were explored and their local minima found. The stoichiometries were chosen by taking all combinations up to 10 atoms per unit cell, the chosen stoichiometries can be seen in the convex hull Figure 1. The 50 lowest energy minima from each stoichiometry are chosen to generate the convex hull. Since MHM uses coarse convergence criteria for geometric relaxation, these structures are reoptimized

with more stringent convergence criteria of 10^{-6} eV for total energies and 10^{-4} eV/Å for forces on atoms.

Phonopy. Phonopy¹⁸ is an open source package for phonon calculations at the harmonic and quasi-harmonic level. The outputs of a VASP calculations are used to produce force constants based on the finite displacement method. From the force constants, thermal properties such as the free energy, entropy, and specific heat are calculated. The Debye frequency is calculated by fitting the lower frequency modes in the density of states with a quadratic fit. The coefficient is then used to calculate the frequency as $\left(\frac{9N}{a}\right)^{1/3}$.

Pyprocar. PyProcar¹⁷ is a robust, open-source Python library used for pre- and postprocessing of the electronic structure data coming from DFT calculations. We use it to analyze data and plot electronic and other properties.

MechElastic. MechElastic is a python script used to calculate elastic properties and perform mechanical stability tests from the elastic constants. It was developed by Singh and Romero.²⁹ It uses the Voigt–Hill method in the calculation of the elastic properties, which is a form of spatial average. In this work, it is used to determine the values found in the elastic property table.

LOBSTER. The LOBSTER code,^{30–33} by the Dronskowski group at RWTH Aachen University, Germany, was used to generate the Crystal Orbital Hamiltonian Population plot (pCOHP). The pCOHP is a method used to partition the band-structure energy as a sum of orbital pair contributions. This allows the generation of a pCOHP diagram which indicates bonding (positive), antibonding (negative), and nonbonding (zero) energy regions in the density of electronic states.

ELATE. ELATE is tensor analysis open source code developed by Gaillac and Coudert at CNRS/Chimie Paris Tec.¹⁶ In this work, ELATE is used to determine the directional dependence of the Poisson ratio and the Negative Linear Compression.

RESULTS AND DISCUSSION

The following sections detail and summarize the calculations performed on the nickel–titanium binary system. In this work, the MHM^{24,25} is used to generate stable crystalline structures comprised of differing stoichiometric ratios of nickel and titanium by sampling points on the potential energy surface. For

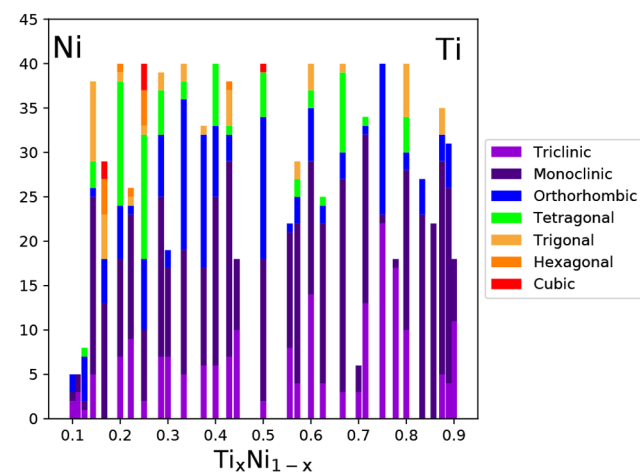


Figure 2. Frequency of each space group obtained in the Ni_xTi_{1-x} structural search for all considered stoichiometries.

this search, 34 different stoichiometries with up to 10 atoms per unit cell were considered. A key difference with other studies is that assumptions about expected crystalline structures are not made, as in the case of crystal combinatorics, nor is the search based on expected bonding types. This is to say, the search is not biased toward previous experimental and theoretical results. Therefore, this method is an efficient representation of the potential energy surface.

Among these structures, the convex hull is determined and two new unreported stable structures are found: an orthorhombic phase with the composition Ni₅Ti and a tetragonal phase for the composition NiTi₂. These phases open the road to novel stoichiometries in this important materials family. Four tetragonal NiTi₂ electronic calculations were performed to compare with the known cubic form. As for the Ni₅Ti structure, bonding and electronic calculations were done to see why there is an increase in strength to the elastic properties. The convex hull is then used to filter structures for further characterization, as only structures on or near the convex hull are usually synthesizable and of interest from an experimental perspective. Within the selected pool of structures, we focus on those with unusual elastic response. Electronic, elastic, bonding, and thermodynamic properties were calculated to provide a complete picture of the mechanical properties over the full phase space. Trends as a function of composition show the 50/50 ratio is maximally anisotropic and weaker, a possible explanation for the observed fatigue failure. The two previously unreported metastable structures with uncommon mechanical properties are revealed by this analysis: The first is a monoclinic NiTi phase which has negative linear compressibility, and the second is a monoclinic phase for NiTi₂ which has negative Poisson ratio.

Convex Hull. The low energy structures obtained from the MHM were reoptimized and used to generate the convex hull: the structures are sorted energetically and their formation energies are obtained with respect to pristine bulk nickel and titanium, to determine chemical stability. This is done by calculating the energy difference per atom with respect to the pure crystal phases. The low-energy structures on the convex hull are kept, which can be seen in the convex hull Figure 1 as the dark blue line connecting the structures. The figure also contains the convex hulls reported in two popular databases, OQMD and the Materials Project (MP),^{34–36} highlighted with dashed green and blue lines, respectively. The database convex hulls are quite close to ours for the known phases, an important benchmark for our calculations, as we use the same software and similar conditions.

The shape memory effect is linked to a martensitic transformation, from a higher energy cubic phase to a low energy monoclinic phase. Among the structures on the convex hull, most compositions support a metastable monoclinic phase; however, only two stoichiometries outside of 50/50 support cubic phases: Ni₂Ti and Ni₅Ti. The Ni₂Ti cubic phase is on the convex hull, so it is unlikely that NiTi₂ supports the shape memory effect. On the other hand, Ni₅Ti has a cubic phase which is metastable and higher in energy than a monoclinic phase, making it a promising candidate for the shape memory effect.

A statistical analysis of the phases was also performed to find general trends. Figure 2 displays the frequency of the crystal structure types found within a $150 \frac{\text{meV}}{\text{atom}}$ cutoff. The majority of structures found are monoclinic and triclinic, but the fraction

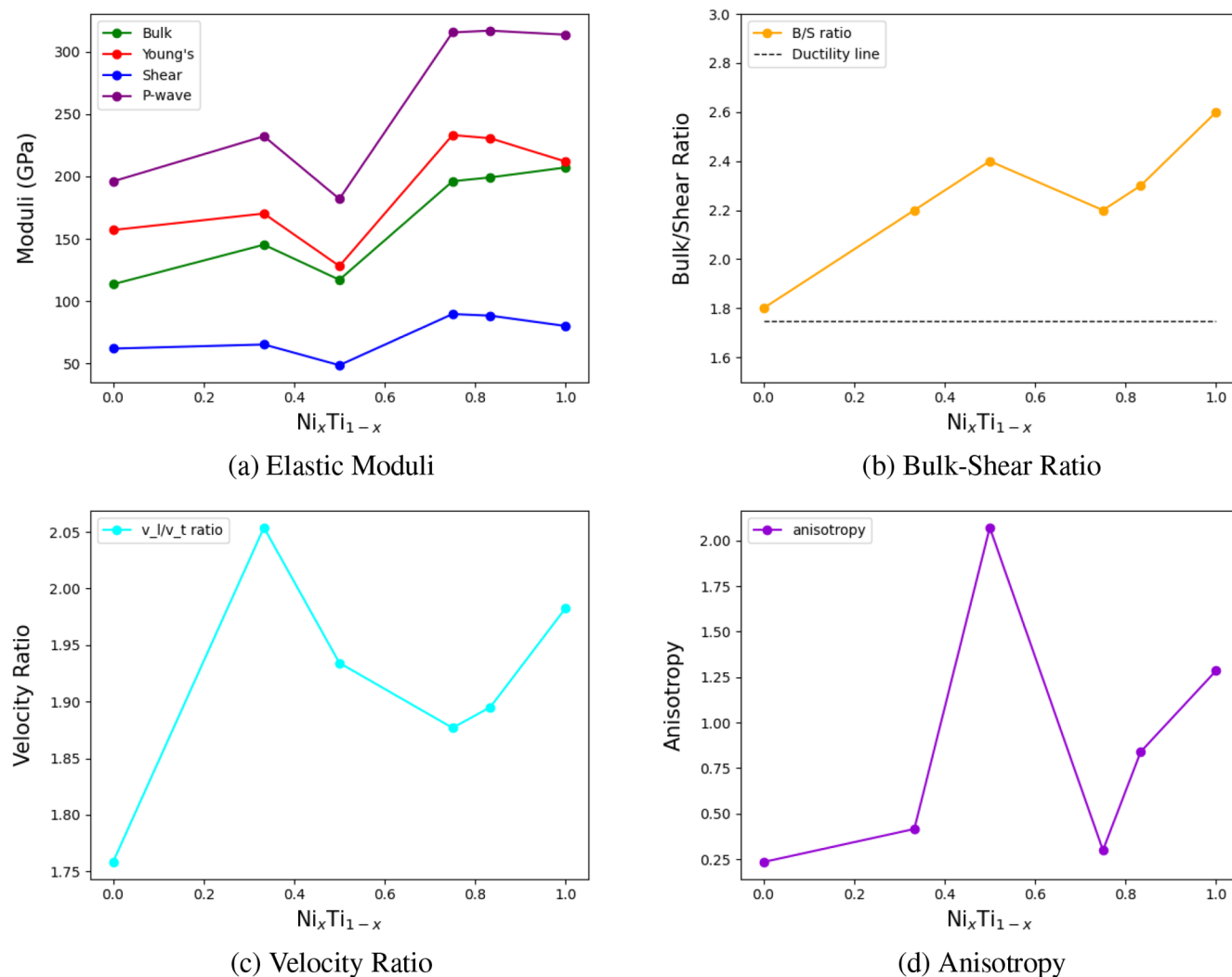


Figure 3. Composition dependence of the elastic properties, for structures near the convex hull. For each composition the properties of the lowest energy phase were used. (a) Enhancement to the P-wave, Shear, and Young moduli from the equi-atomic composition. For nickel-rich composition this enhancement is greater than the nickel pristine case. The trend in the P-wave, Shear, and Young's moduli corresponds to the anisotropy (c) and the sound velocity (d) ratios. Higher anisotropy and velocity ratios indicate lower values in these moduli. (b) All structures are considered ductile since they lie above the value of 1.75 as mentioned by Pugh.³⁸

depends on the Ni/Ti ratio. The only cubic structures found, other than the equiatomic case, are in the Ni-heavy region (pure Ni is FCC). Tetragonal and hexagonal structures are also primarily found in the Ni-rich region, with the exception of some tetragonal phases for NiTi_3 . Overall, there is a large diversity of crystal families in the nickel region, while in the titanium region, the majority of the structures have very low symmetry.

Only structures within 50 meV/atom of the convex hull are selected for further characterization to ensure they have a chance of being synthesized experimentally. In order to ensure accurate values for physical properties, further geometric relaxation is performed on these structures, as discussed in the computational details section. The process of finding structures of interest can be thought of as a series of filters, in which a smaller number of structures are chosen at each step of the process, to be converged with finer tolerances and more advanced properties. This is done for the sake of computational efficiency.

Of the filtered results, four compositions are found with structures on the convex hull: NiTi_2 , NiTi , Ni_3Ti , and Ni_5Ti . The SI contains the crystallographic information for the

structures on the convex hull, and also includes the low energy structures for these compositions found in OQMD, MP, and experimental studies. For NiTi and Ni_3Ti compositions, the structures found using MHM are in agreement with previous results. For Ni_2Ti , a tetragonal structure with space group $I4/mmm$ was found, which is lower in energy than the previously reported $Fd\bar{3}m$ structure. Finally, a structure is found on the convex hull for a previously unreported composition, Ni_5Ti with space group $Cmmm$. For each structure on the convex hull, the phonon dispersion curves are positive, indicating dynamical stability (see the SI). Additionally, with the help of the MechElastic code,^{29,37} we verify that the elastic constants of each convex hull structure satisfy the Born criteria, which indicates mechanical stability.

Elastic Properties. The elastic properties of all structures found on the convex hull are displayed in a table in the SI and were determined through the open-source MechElastic python script.^{29,37} Some general trends can be extracted from the table based on composition. The most striking feature is the decrease of the moduli near the equiatomic ratio. This relation indicates

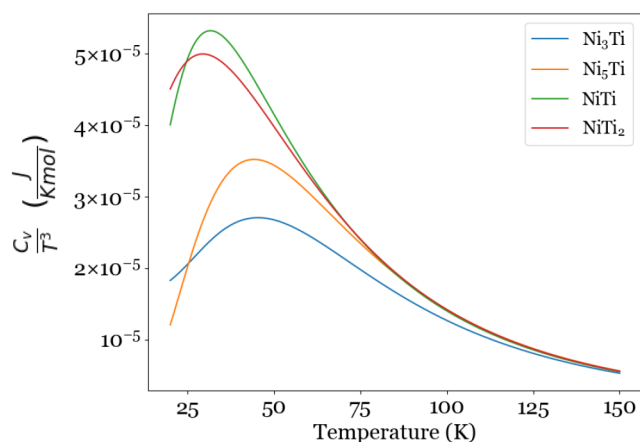
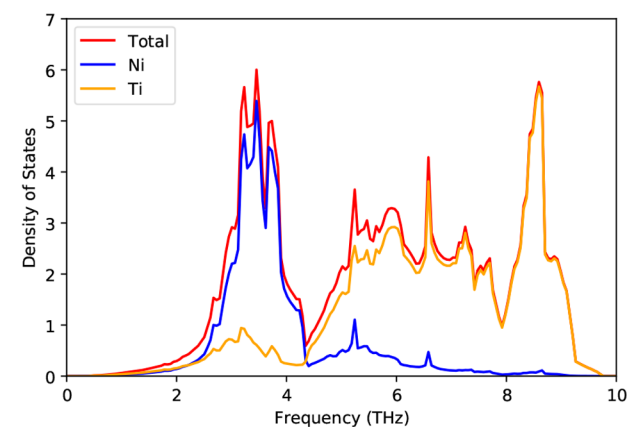


Figure 4. C_v/T^3 for structures on the convex hull. The temperature starts at 20 K and all curves go to a constant at 0 K as expected from theory. These curves show the thermal activation of optical and acoustic phonon modes for the different structures. The peak is caused by the combination of the acoustic and optical phonon modes.

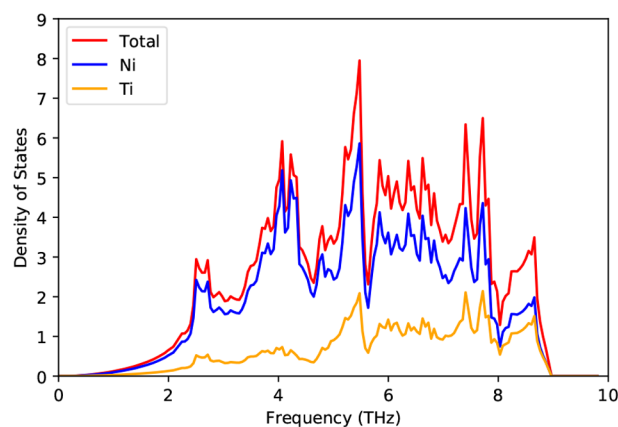
the weakness of the 50/50 alloy and explains the previously reported sensitivity to massive strains. Segregation of either titanium or nickel enhances the moduli, and nickel enrichment

even enhances the moduli beyond pristine Ni, which can be seen in Figure 3a).

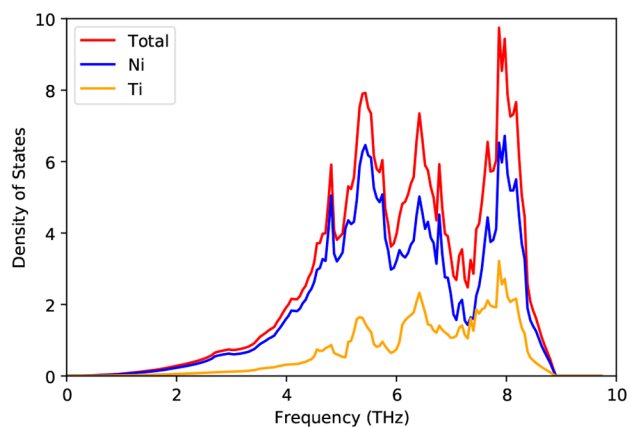
Two measures of anisotropy are also displayed in the elastic properties tables in the SI, the universal anisotropy,³⁹ and the log-Euclidian anisotropy.⁴⁰ The anisotropy formulas are in eqs 1 and 2, respectively. Here, G and K are the shear and bulk modulus, and the V and R superscripts are the Voigt and Reuss estimations, respectively. For universal anisotropy, the larger the deviation from zero, the more anisotropic a material is. This scale is relative to a limiting value for a single crystal and thus cannot be compared as simply between materials. The Log-Euclidian anisotropy is designed to do just this. For structures on the convex hull, both measures of anisotropy yield the same ordering of structures, from least to most anisotropic: hexagonal Ni_3Ti , tetragonal Ni_2Ti , orthorhombic Ni_5Ti , and finally orthorhombic NiTi . This ordering is not surprising, as the least anisotropic materials have higher symmetry. Figure 3d is the anisotropy composition dependence. Comparing with the other plots in the figure, the same trend occurs in the sound velocity and bulk/shear ratios. Interestingly enough, there is a correspondence between higher anisotropy and the weakening of the Young, shear, and P-wave moduli at equi-composition. This indicates that the behavior predicted from the elastic



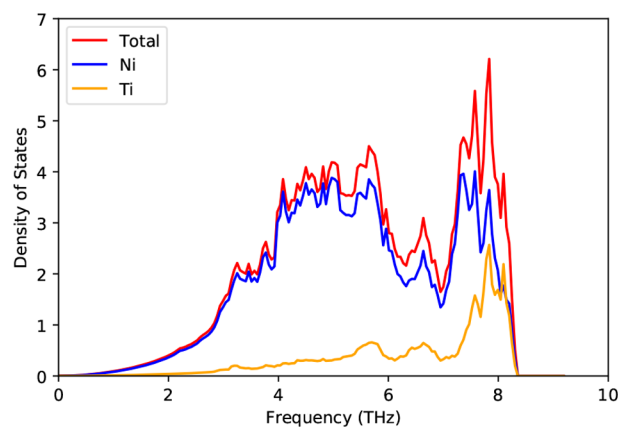
(a) NiTi_2 $I4/mmm$



(b) NiTi $Pnma$



(c) Ni_3Ti $P6_3/mmc$



(d) Ni_5Ti $Cmmm$

Figure 5. Phonon density of states (in units of $(\text{states}/\text{\AA}^3 \text{ THz})$) for convex hull structures. In all panels, Ni modes dominate the lower frequency modes; therefore, low-temperature responses are primarily from the Ni–Ni bonds. As the Ni fraction increases, Ni modes begin to dominate over a wider frequency range.

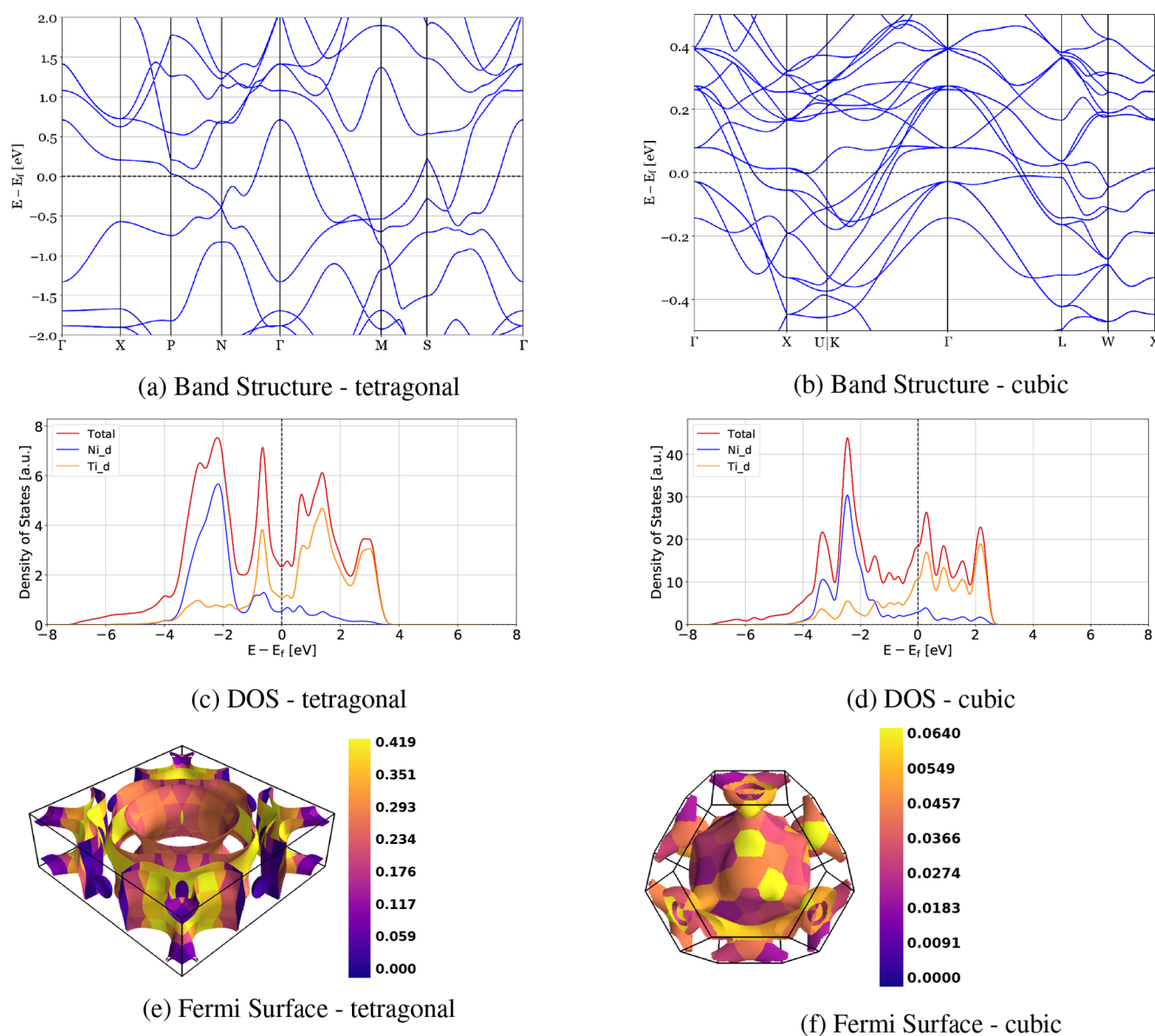


Figure 6. NiTi₂ comparison of electronic properties. The first column shows the predicted tetragonal structure and the second column shows the previously reported cubic structure. The differences between the two structures can be seen in each row. One noticeable difference is the shifting of the titanium DOS peak just below the Fermi level in (c) up to that of the cubic case. (e, f) Fermi surfaces of the two structures. The color scale stands for different bands that compose the surface. The surfaces suggest vastly different electron transport. The tubular nature of (e) shows 2D in-plane transport, whereas the cubic case shows a highly connected roughly spherical surface which is typical of transition metals.

constants is also supported by the vibrations, as we should expect.

$$A^U = 5 \frac{G^V}{G^R} + \frac{K^V}{K^R} - 6 \quad (1)$$

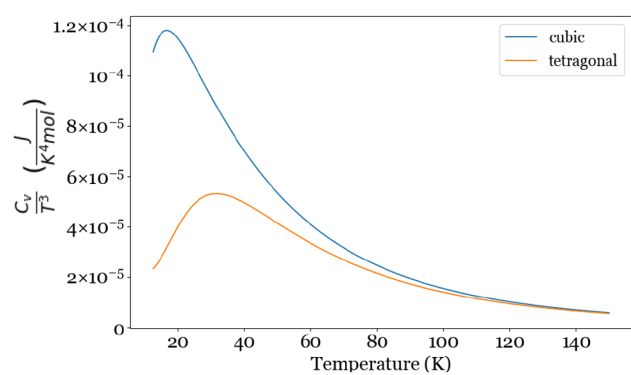
$$A^L = \sqrt{5 \left[\ln \left(\frac{G^V}{G^R} \right) \right]^2 + \left[\ln \left(\frac{K^V}{K^R} \right) \right]^2} \quad (2)$$

Other than the monoclinic NiTi structure, the spatially averaged Poisson ratio is roughly the same for every structure. This means that the perpendicular elastic response of the crystal with respect to a uniaxial strain is almost independent of the stoichiometry for the convex hull structures.

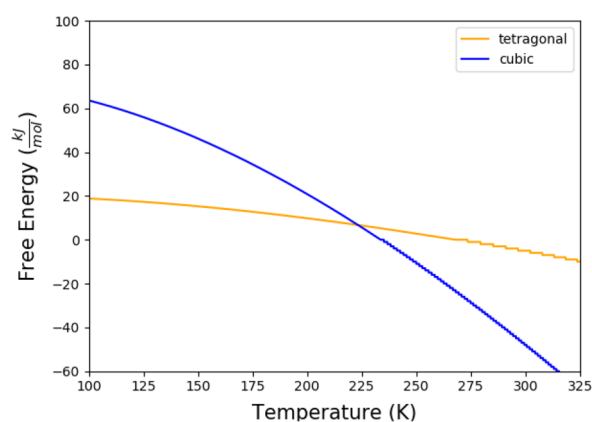
The B/S ratio is an indicator of the brittleness/ductile behavior of a material as proposed by Pugh,³⁸ where a high ratio

indicates ductility and a low ratio indicates brittleness. The critical value separating whether a material is brittle or ductile is 1.75. Observing the plot in Figure 3b, all convex hull structures are above the critical ductile line, making them more ductile than brittle. Tungsten, which has the highest tensile strength of any natural material, has significantly larger values for its elastic properties than any of the convex hull structures but is less ductile. It is also interesting to compare the properties of the Ni-rich region to stainless steel. Both Ni₃Ti and Ni₅Ti have enhanced elastic properties relative to stainless steel, with comparable ductility.

The most interesting trend that can be drawn from elastic properties is the increase of the moduli for high nickel concentration, which is promising for strengthening materials in structural engineering applications. As previously mentioned, the Young, shear, and P-wave moduli values are even higher than



(a) Heat capacity Temperature dependence



(b) Free Energy/Temperature dependence

Figure 7. Thermodynamics of NiTi₂ phases. (a) Differences between the heat capacity at low temperature, which gives an indication of the relevant roles of acoustic and optical phonons in each structure. (b) Differences in free energy near room temperature. The cubic phase has a significantly lower free energy, leading it to be more thermodynamically favorable than the tetragonal phase.

pristine nickel. This is examined below in the Ni₅Ti section, where the bonding nature is studied in detail to gain a better understanding of the enhancement.

Thermodynamic Properties. Thermodynamic properties have been calculated for all of the structures on the convex hull, through the phonon dispersion relations and the density of states, using PHONOPY.¹⁸ It should be noted this harmonic analysis neglects the contribution from the conduction electrons and phonon anharmonicity. The temperature dependence of the heat capacity was calculated and the results are captured in Figure 4, where the C_v/T^3 curves are shown for the hull phases: hexagonal Ni₃Ti, tetragonal Ni₂Ti, orthorhombic Ni₅Ti, and orthorhombic NiTi.

The low temperature regime corresponds to acoustic mode contributions which leads to a T^3 behavior of C_v . In a second regime (20–60 K roughly), the higher lying optical modes create the observed broad peaks. The peak position is a consequence of the particular optical mode frequencies, when they begin to dominate C_v , and when the full manifold of phonons is saturated as $k_B T > \omega_{\max}$. For NiTi₂, NiTi, Ni₃Ti, and Ni₅Ti, the peaks occur at 35, 30, 50, and 35 K, respectively.

This maximum can be tuned by changing the isotopic concentration, as it has been experimentally demonstrated in ZnO⁴¹ and Boron.⁴² For example nickel can have stable isotopes of ⁵⁸Ni, ⁶⁰Ni, ⁶¹Ni, ⁶²Ni, and ⁶⁴Ni⁴³ and titanium has ⁴⁴Ti, ⁴⁶Ti,

⁴⁷Ti, ⁴⁸Ti, ⁴⁹Ti, and ⁵⁰Ti⁴⁴ (experimentally it is even possible to go up to ⁸⁰Ni and ⁶³Ti). The peak position and magnitude can be related through a simple relation in the harmonic approximation as discussed in ref.⁴⁵ Isotopic manipulation is very expensive and is not industrially feasible, but it is an interesting route to check different processes and dispersions we derive here.

In the high temperature regime all modes contribute to C_v , and the heat capacity tends to the Dulong and Petit constant value (universal in the harmonic approximation). In this regime, C_v/T^3 will decay with a T^{-3} power law.

Figure 4 indicates that the phonon density of states deviates quickly from the ideal Debye model, where the phonon density of states follows $D(\omega) = A\omega^2$ and C_v/T^3 would be constant at low T . The change in contributions to the thermal response as a function of composition can be seen in the phonon density of states as in Figure 5. For all four structures, Ni contributes more to the low-frequency modes. This means the thermal response of these systems is primarily influenced by contributions from the heavier Ni atoms. In the $I4/mmm$ (Figure 5a), all of the Ni modes are restricted to the lower frequencies; the vast difference in phonon distribution is an indicator of a different kind of bonding mechanism. As the Ni fraction increases (i.e., number of Ni–Ni bonds grows); in turn, the Ni modes dominate over wider frequency range.

Ground-State NiTi₂ $I4/mmm$. From both databases OQMD and MP^{34–36} and experiment,⁴⁶ the known phase for NiTi₂ is a structure with space group symmetry $Fd\bar{3}m$. Here, another structure is found on the convex hull with space group $I4/mmm$. It has a formation energy per atom of -7.49 eV/atom, which is lower than the known FCC phase, whether using PBE or LDA functionals. In both OQMD and MP databases, there are 24 atoms in the primitive cells for $Fd\bar{3}m$, which puts the structure outside the search space of our MHM, as only cells of up to ten atoms were considered. Standalone calculations were performed for the 24 atom $Fd\bar{3}m$ structure, with initial structural information from the Materials Project. The new $I4/mmm$ structure on our convex hull is still 22.8 meV/atom lower in energy than the cubic phase. To differentiate between the cubic $Fd\bar{3}m$ and tetragonal $I4/mmm$ phases, the mechanical and thermal properties of both structures are determined and compared. For the $Fd\bar{3}m$ phase, the results are in agreement with the literature and previous works.⁴⁷ There is a difference in the Young and shear moduli, where the new $I4/mmm$ phase is significantly larger in comparison to the $Fd\bar{3}m$ phase. The cubic phase has been reported experimentally;^{34–36,46} however, the tetragonal phase has not even though it has lower total energy. The heat capacities near room temperature are nearly identical for both the $I4/mmm$ and $Fd\bar{3}m$; this complicates the identification of the unique NiTi₂ phase, so other methods are necessary for characterization. X-ray diffraction would be a natural characterization scheme, and we provide the XRD data for both structures in the SI. As for the synthesis process, there is a thermodynamic competition between the cubic and tetragonal phases at high temperature, which is shown in the free energy-temperature dependence in Figure 7b. The cubic phase is lower in free energy than the tetragonal phase at high T , which is probably why the tetragonal phase has not been previously synthesized in experiments.

Figure 7a depicts the difference in C_v/T^3 for crystal phases. First, the Einstein peak intensity is much larger in the $Fd\bar{3}m$ phase and it is located at a lower temperature: 25 K in the cubic structure and 35 K for tetragonal. Additionally, the C_v/T^3 decay from that peak (constant C_v at higher temperatures) is slower in

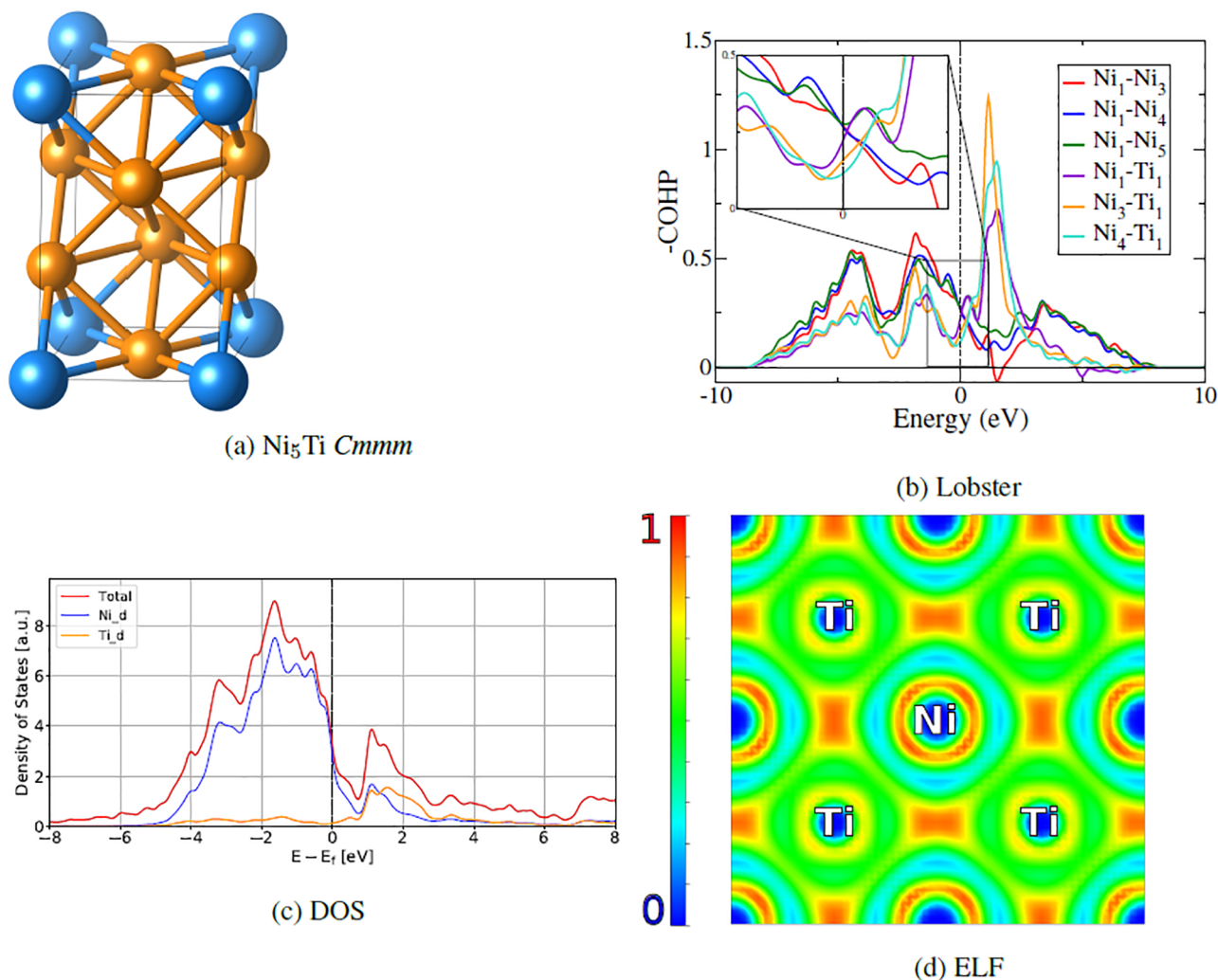


Figure 8. Analysis for the enhanced elastic properties for Ni_5Ti . The enhanced elastic properties can be attributed to the increase amount of Ni–Ni bonds in the structure. From subFigure 8b shows the Ni–Ni bonds are stronger than the Ni–Ti bonds at the Fermi energy. The contribution of nickel to the bonding further evidenced by nickel atoms dominating around the Fermi energy in the density of states and the increased electron localization in between the nickel atoms from (c) and (d), respectively.

the $I4/mmm$ phase. This indicates that thermal excitations of higher frequency optical phonons require larger temperatures to equilibrate.

The band structures and density of states plots of each phase are generated using Pyprocar¹⁷ and displayed in Figure 6a,b,c,d, respectively. One can immediately notice the large differences between the two band structures. The number of bands are related to the number of ions in the unit cell. The cubic phase was calculated with 24 ions and the tetragonal phase was calculated with six ions.

In both cases, the density of states is spin degenerate, and the sum of both spin channels is displayed in this figure. The new $I4/mmm$ phase shows a large jump in the occupied Ti d-states just above the Fermi level. The main contribution to the DOS both below and above the Fermi level comes from Ti d electrons. At the Fermi level, it can be seen that the Ni and Ti d states hybridize and have comparable DOS, with the first Ti peak just below/above E_F in the tetragonal/cubic cases. To help illuminate where the differences are coming from, the local atomic-structures of both phases are examined in a supercell using the VESTA software.⁴⁸ The cubic phase is formed by small clusters of Nickel atoms embedded in Titanium, where as the

tetragonal phase forms 2D layers of Nickel and Titanium atoms. The formation of these microstructures is linked to bonding geometry and type, and causes the stark differences seen in the XRD, band structures, and the density of states.

The Fermi surfaces of both phases are displayed in Figure 6e,f and are in agreement with the properties of the local structural topology discussed before. The layered nature of the tetragonal phase yields a tubular FS indicating predominantly 2D or layered in-plane transport. The cubic phase, however, is more clustered with no layering. The Fermi surface is highly connected and roughly spherical with some lobes, which is typical of transition metals. The transport properties of the two phases should be very different and easy to distinguish experimentally in single crystals.

Ground-State Ni_5Ti $Cmmm$. A new structure on the convex hull was found using MHM with a total energy of -6.433 eV/atom, with the composition Ni_5Ti and space group $Cmmm$. This structure was previously unreported in the literature, even though it is both dynamically and mechanically stable. As discussed above, its elastic properties are enhanced beyond those of pristine Ni and Ti.

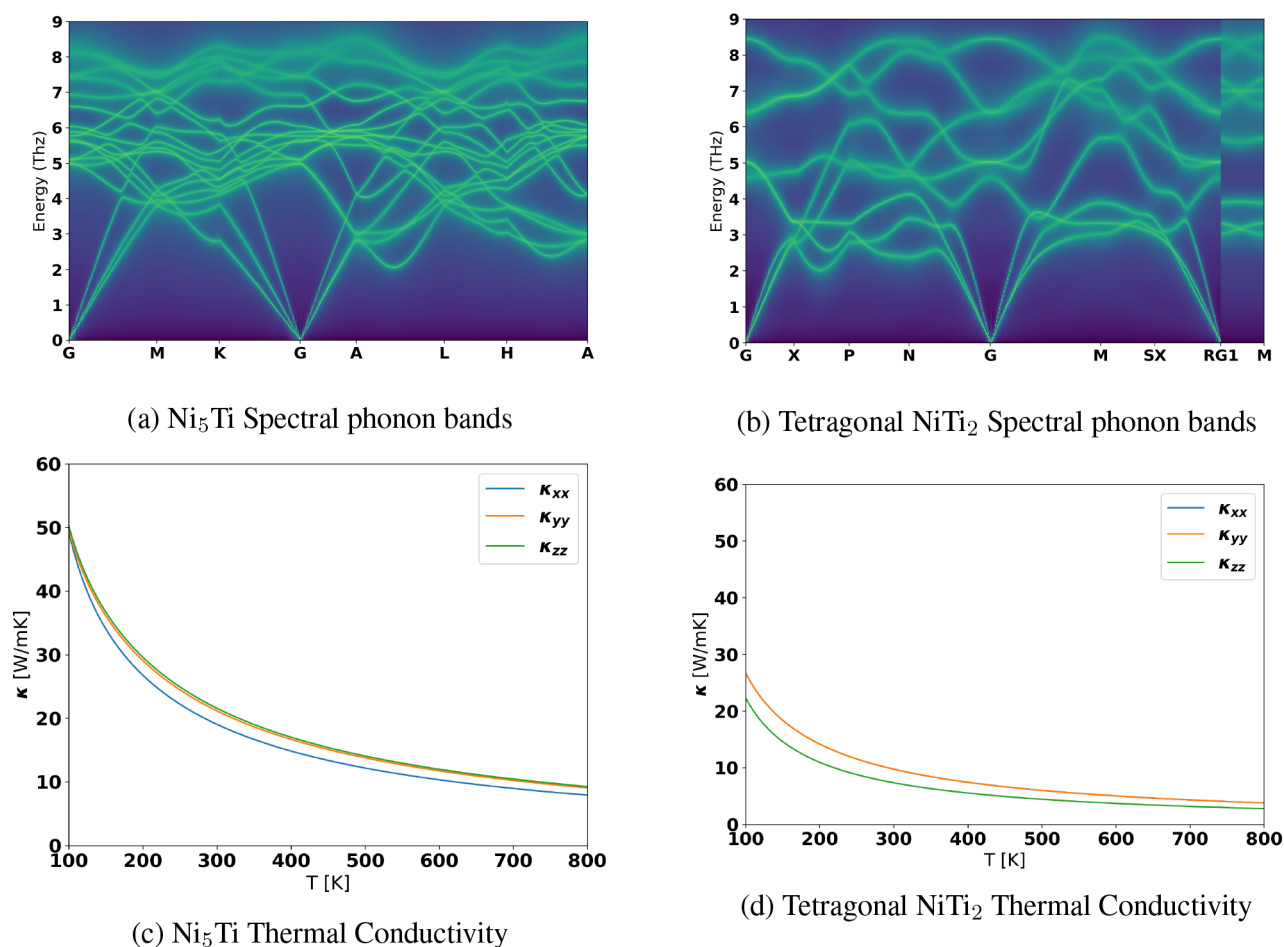


Figure 9. Effect of anharmonicity for Ni_5Ti and NiTi_2 within the TDEP method. (a, b) Spectral phonon dispersion plot. (c, d) Temperature dependence of the thermal conductivity at 600 K.

This enhancement primarily stems from Ni–Ni bonds in the [001] plane. This can be seen from the pCOHP displayed in Figure 8b. In this plot, the bond contributions between pairs of Ni and/or Ti atoms are displayed. At the Fermi energy, contributions from pairs of Ni atoms in the [001] plane dominate, which may be more easily seen in the inset plot. The Ni–Ni bonds contribute more to the COHP than the Ni–Ti bonds at the Fermi level.

This can further be seen in the Electron Localization Function (ELF) plot in Figure 8d, as there is strong electron localization between pairs of Ni atoms. The density of states plot in Figure 8c shows the enhancement comes from the Ni–Ni bonds. The primary contribution to the total DOS at the Fermi level is from Ni *d*-states.

To finish our discussion about the two new low energy stable phases we have calculated the anharmonic effects into the phonon spectra (the spectral phonon dispersion $A(\mathbf{Q}, E)$) for both Ni_5Ti and NiTi_2 ; thus, obtaining the renormalized phonon dispersion at 600 K, the phonon–phonon line width, and temperature-dependent thermal conductivity. These results are important to gauge how well the temperature-dependent effective potential TDEP models these structures when comparing to inelastic neutron-scattering experiments. For Ni_5Ti phonon spectrum shows no phonon softening with *T*. The optical phonon line widths are broader than for acoustic modes as seen in Figure 9a, which is expected as the former have more decay channels. As for the NiTi_2 phonon spectrum in 9b, we

observe strong diffusion of some of the lines in the spectra, especially to the low energy optical modes at the γ point. This tells us anharmonicity plays an important role in the determination of temperature dependent quantities in this structure. The temperature-dependent thermal conductivities are shown in Figure 9c,d. Ni_5Ti has a larger conductivity than NiTi_2 , which can be correlated to the increase in the number of nickel–nickel bonds in a material. At 300 K, the conductivities for Ni_5Ti and NiTi_2 are around 20 and 10 W/mK, respectively. These are moderate conductivity values: extreme values are found in materials such as glass (0.1 W/mK), iron (80 W/mK), or silicon (130 W/mK).

Metastable Structures with NLC and NPR. In addition to the new convex hull structures found, there are two metastable cases which have exotic elastic properties. For the composition NiTi, a monoclinic structure with space group $P2/m$ was found to possess negative linear compressibility. Additionally, a monoclinic phase was found for NiTi_2 in space group $C2/m$, with a negative Poisson ratio. Both properties are of interest for technological applications, and are quite rare in nature: In the work by Dagdelen et al.,⁴⁹ over 67000 structures from the Materials Project were screened to determine which were auxetic candidates. Only 38 structures were found from this screening, and when the elastic constants were calculated explicitly only eight were truly auxetic. It must be noted, however, that in the initial screening done by Dagdelen the elastic constants were calculated through the Voigt and Hill

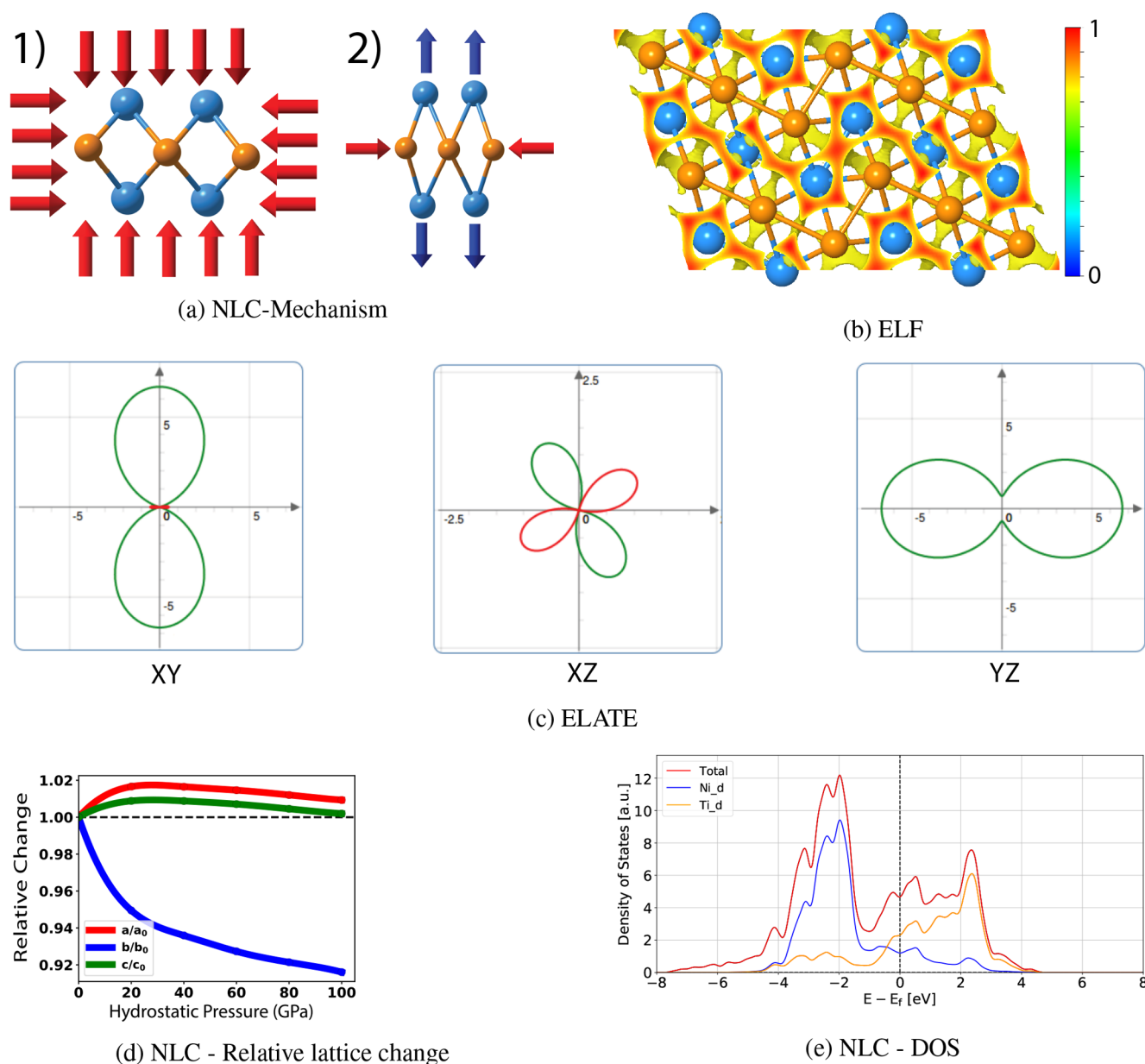


Figure 10. Negative linear compression. (a) Mechanism for NLC in NiTi with space group $P2_1/m$. Ti atoms are blue and Ni atoms are orange. (1) The red arrows here represent Forces. (2) The arrows here represent directions of length change, where the red and blue represent a decrease and an increase, respectively. Only the [101] plane is shown, as the cell decreases in length, normally along the [010] direction increases. (b) Electron localization function. (c) Directional dependence of the NLC. Green curves display positive linear compressibility, and red curves display negative linear compressibility. The maximal negative value occurs in the XZ plane. (d) Relative change in the lattice parameters under hydrostatic pressures of 2, 4, 6, 8, and 10 GPa. (e) Density of states of NiTi.

method. This method is a form of a spatial average, and the resulting elastic properties do not give any indication whether they are anisotropic or not. Any system with highly anisotropic behavior would not be flagged, which offers some hope that many more auxetics and NLC may exist. The two new phases found in this work are now examined in more detail.

NiTi $P2_1/m$ with NLC. The MHM study identified the metastable phase NiTi with space group $P2_1/m$ presenting negative linear compressibility (NLC). It has a total energy of -7.08 eV/atom, 161 meV/atom above the ground state. The elastic properties of this phase are listed in the elastic table in the SI. The Bulk, shear, and Young moduli are comparable to those of the B19' phase ($P2_1/m$), which has been identified as the

stable phase of NiTi at room temperature. Because of this, the B/S ratio is nearly identical as well, and thus, the phase is ductile. The elastic moduli and their directional dependence were determined with the ELATE software package:⁵⁰ while their average values are positive, they are quite anisotropic. The directional dependence of the linear compressibility is displayed in Figure 10c. From this analysis, the NLC has a maximal negative value in the $a-c$ plane of -4.1732 TPa⁻¹, directed along the unit vector $(-0.89, 0.00, -0.46)$. For comparison, in the rutile structure class, TeO₂ displays the maximal NLC value of -5.1 TPa⁻¹. BiB₃O₆, which displays NLC due to a tilted network mechanism, has been shown experimentally to reach -12.5

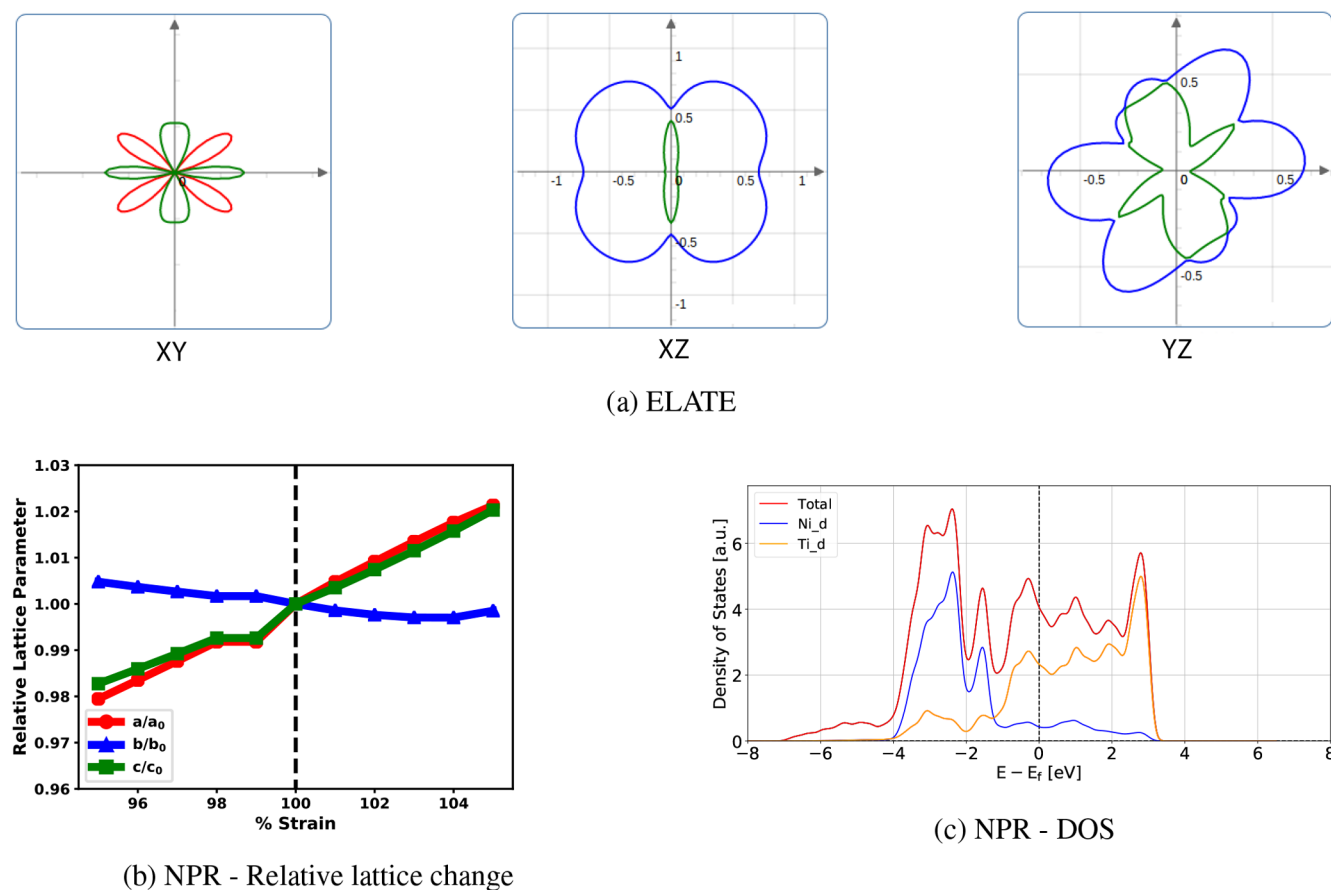


Figure 11. Negative Poisson ratio. (a) Spatial dependence of Poisson's ratio for NiTi₂ with space group C2/m. (c) The red curve is the minimal NPR, green is the positive Poisson ratio. (b) Relative change in the lattice parameters under strain applied along the (0.75, 0.45, -0.49) direction. Both the *a*-axis and *c*-axis have an auxetic response to the applied strain. (c) Density of states for NiTi₂ with space group C2/m.

TPa⁻¹. An even larger value of -42 TPa⁻¹ was found in zinc dicyanoaurate Zn[Au(CN)₂]₂.⁵¹

To show the mechanism is not unique to the particular choice of Ni and Ti, additional calculations are performed with other common intermetallic elements. The elements chosen were Ag, Cd, Cu, Zn, Mn, and Nb. Out of all substitutions performed, only NiMn yielded a stable structure with the same crystalline lattice. NiMn also displays NLC, which is similar in character to NiTi.

Constrained relaxation of the crystal structures within DFT allow for the determination of changes in interatomic distances and cell parameters under applied hydrostatic pressure. Under positive pressure, the unit cell *increases* in length in the *a* and *c* directions, whereas it decreases in the *b* direction. This behavior is better visualized in Figure 10d. An increase in the *a* and *c* cell parameters would indicate an increase in area; however, as stress is applied, the angle between *a* and *c* decreases sufficiently to yield an overall shrink in the area of the *a*-*c* plane. This implies that the NLC is not along the crystalline axes (in agreement with the direction of maximal NLC found with ELATE). This is expected, as the structure has monoclinic symmetry.⁵²

The mechanism for NLC is displayed in Figure 10a. Under hydrostatic strain, Ni atoms in the [101] plane are forced closer together; in turn, this pulls the Ti atoms in this plane further apart, which is similar to the well-known wine-rack model. The ELF plot in Figure 10b shows this behavior occurring. A strong electron localization is observed between pairs of Ti atoms in the

[101] direction, with no localization between pairs of Ni atoms. Due to the strong bonding between Ti atoms along [101], the distance between them remains fixed. The contraction of Ni-Ni bonds forces Ti atoms further apart along the [-102] direction. More evidence for the effect is found in the density of states (Figure 10e), as the Ti d-states are more highly occupied at the Fermi level, coherent with the ELF.

NiTi₂ C2/m with NPR. An auxetic structure was found for the NiTi₂ composition with space group C2/m and total energy -7.43 eV/atom, which is 60 meV/atom above the ground state. It must be stressed this auxetic response is directional dependent; the value that appears in the elastic properties table in the SI is the spatial average, which ignores directionality. The ELATE software package⁵⁰ was used to determine the angular dependence of elastic properties, displayed in Figure 11a. The maximal negative Poisson ratio is calculated to be -0.31 directed along the unit vector (0.75, 0.45, -0.49). For comparison, a NPR of around -0.03 has been reported in carbon nitride.⁵³ In α -SiO₂, the maximum known NPR value is -0.59.⁵⁴

A constrained relaxation was performed under both tensile and compressive strain to determine the lattice constants and interatomic distances. Both types of strain were applied along the unit-vector where the Poisson ratio attains its maximum value. Figure 11b displays the relative change in the lattice parameters under applied strain. Both the *a*-axis and *c*-axis decrease when compressive strain is applied, and vice versa for

tensile strain. This is precisely the response expected from an auxetic material.

The electronic density of states for this phase is displayed in Figure 11c. The Ti *d* electrons are the primary contribution to the density of states at the Fermi level. In addition, they are the primary contribution just below the Fermi level (>2 eV) and above the Fermi level. At lower energies, the Ni *d* electrons dominate.

CONCLUSIONS

To conclude, minima on the potential energy surface of various compositions of the binary system NiTi were located through the use of the minima hopping method, searching for other stoichiometries with novel stable phases, exotic elastic properties, and other conditions presenting the shape memory effect. These minima, combined with the pristine structures for both elements, were used to construct a more complete convex hull. It was identified that Ni₅Ti and NiTi are the only compositions that have the necessary high energy cubic phase and lower energy monoclinic phase. Both stable and metastable structures within 50 meV of the convex hull were identified, and derived physical properties were calculated. For the structures found on the convex hull, those with the composition NiTi and Ni₃Ti are in agreement with previous experimental and theoretical results. For the composition NiTi₂, a new structure with space group *I4/mmm* is found, which is lower in energy than the previously reported *Fd3m* structure (by 22.8 meV/atom). From the new ground state to the predicted one, different behaviors in the heat capacity and Fermi surface were found, which can be used to discriminate the existence of this phase. A new structure is found on the convex hull with the composition Ni₅Ti, in space group *Cmmm*, that has elastic properties enhanced beyond the pristine cases. Two monoclinic metastable structures were also identified with interesting mechanical properties: a structure with composition NiTi which displays negative linear compressibility, and another with composition NiTi₂, which displays a negative Poisson ratio. The NLC in the NiTi structure has a similar mechanism to that described for cubic metals by Baughman et al.⁵⁵ The anisotropy of these exotic elastic properties gives hope that many more auxetic materials can be found, beyond those identified in the study by Dagdelen et al.⁴⁹

ASSOCIATED CONTENT

Supporting Information

The following file is available free of charge. The Supporting Information is available free of charge at <https://pubs.acs.org/doi/10.1021/acs.jpcc.0c10453>.

Tables containing crystallographic information, elastic properties, and thermal properties for already reported and new structures found in this study; phonon dispersion curves, CIF data, and XRD plots generated by VESTA (PDF)

AUTHOR INFORMATION

Corresponding Authors

Logan Lang – Department of Physics, West Virginia University, Morgantown, West Virginia 26506, United States;
orcid.org/0000-0003-2867-1706; Email: llang@mix.wvu.edu

Adam Payne – Department of Physics, West Virginia University, Morgantown, West Virginia 26506, United States;

orcid.org/0000-0002-3735-0405; Email: apayne9@mix.wvu.edu

Irais Valencia-Jaime – Department of Physics, West Virginia University, Morgantown, West Virginia 26506, United States; Email: iraisvj@gmail.com

Matthieu J. Verstraete – NanoMat/Q-Mat/CESAM and European Theoretical Spectroscopy Facility, Université de Liège (B5), B-4000 Liège, Belgium; Catalan Institute of Nanoscience and Nanotechnology (ICN2), Campus UAB, Bellaterra 08193, Barcelona, Spain; Email: matthieu.verstraete@uliege.be

Alejandro Bautista-Hernández – Facultad de Ingeniería, Benemérita Universidad Autónoma de Puebla, CP. 72570 Puebla, Mexico; Email: alejandro.bautista@correo.buap.mx

Aldo H. Romero – Department of Physics, West Virginia University, Morgantown, West Virginia 26506, United States; Facultad de Ingeniería, Benemérita Universidad Autónoma de Puebla, CP. 72570 Puebla, Mexico; orcid.org/0000-0001-5968-0571; Email: aldo.romero@mail.wvu.edu

Complete contact information is available at: <https://pubs.acs.org/10.1021/acs.jpcc.0c10453>

Notes

The authors declare no competing financial interest.

ACKNOWLEDGMENTS

We acknowledge the computational resources awarded by XSEDE, a project supported by National Science Foundation Grant No. ACI-1053575. We acknowledge the support from the Texas Advances Computer Center (with the Stampede2 and Bridges supercomputers). This work was supported by the DMREF-NSF 1434897, NSF OAC-1740111, and DOE DESC0021375 projects. M.J.V. acknowledges funding by the Belgian FNRS (PDR G.A. T.1077.15-1/7, T.0103.19, and a sabbatical “OUT” grant at ICN2), ULiege, and the Communauté Française de Belgique (ARC AIMED G.A. 15/19-09) and computational resources from the Consortium des Equipements de Calcul Intensif (FRS-FNRS G.A. 2.5020.11) and Zenobe/CENAERO funded by the Walloon Region under G.A. 1117545.

REFERENCES

- (1) Favier, D.; Liu, Y.; Orgeas, L.; Sandel, A.; Debove, L.; Comte-Gaz, P. Influence of Thermomechanical Processing on the Superelastic Properties of a Ni-Rich Nitinol Shape Memory Alloy. *Mater. Sci. Eng., A* **2006**, *429*, 130–136.
- (2) Gallardo Fuentes, J. M.; Gümpel, P.; Strittmatter, J. Phase Change Behavior of Nitinol Shape Memory Alloys. *Adv. Eng. Mater.* **2002**, *4*, 437–452.
- (3) McKelvey, A.; Ritchie, R. Fatigue-Crack Growth Behavior in the Super-Elastic and Shape-Memory Alloy Nitinol. *Metall. Mater. Trans. A* **2001**, *32*, 731–743.
- (4) Ferreira, M. d. A.; Luersen, M. A. A.; Borges, P. C. A. Nickel-titanium Alloys: A Systematic Review. *Dental Press J. Orthod.* **2012**, *17*, 71–82.
- (5) Huang, X.; Bungaro, C.; Godlevsky, V.; Rabe, K. M. Lattice Instabilities of Cubic NiTi from First Principles. *Phys. Rev. B: Condens. Matter Mater. Phys.* **2001**, *65*, No. 014108.
- (6) Marcinkowski, M. J.; Sastri, A. S.; Koskimaki, D. Martensitic Behaviour in the Equi-Atomic Ni-Ti Alloy. *Philos. Mag.* **1968**, *18*, 945–958.
- (7) Golestaneh, A.; Carpenter, J. Study of the Martensitic Transformation in Shape-Memory Nitinol Alloy by Time-of-Flight Neutron Diffraction Techniques. *Acta Metall. Mater.* **1990**, *38*, 1291–1305.

- (8) Zeng, Z.-Y.; Hu, C.-E.; Cai, L.-C.; Chen, X.-R.; Jing, F.-Q. Lattice Dynamics and Phase Transition of NiTi Alloy. *Solid State Commun.* **2009**, *149*, 2164–2168.
- (9) Kresse, G.; Hafner, J. Ab Initio Molecular Dynamics for Liquid Metals. *Phys. Rev. B: Condens. Matter Mater. Phys.* **1993**, *47*, 558–561.
- (10) Kresse, G.; Hafner, J. Ab Initio Molecular-Dynamics Simulation of the Liquid-Metal–Amorphous-Semiconductor Transition in Germanium. *Phys. Rev. B: Condens. Matter Mater. Phys.* **1994**, *49*, 14251–14269.
- (11) Blöchl, P. E. Projector Augmented-Wave Method. *Phys. Rev. B: Condens. Matter Mater. Phys.* **1994**, *50*, 17953–17979.
- (12) Kresse, G.; Furthmüller, J. Efficiency of Ab-Initio Total Energy Calculations for Metals and Semiconductors using a Plane-Wave Basis Set. *Comput. Mater. Sci.* **1996**, *6*, 15–50.
- (13) Perdew, J. P.; Chevary, J. A.; Vosko, S. H.; Jackson, K. A.; Pederson, M. R.; Singh, D. J.; Fiolhais, C. Atoms, Molecules, Solids, and Surfaces: Applications of the Generalized Gradient Approximation for Exchange and Correlation. *Phys. Rev. B: Condens. Matter Mater. Phys.* **1992**, *46*, 6671–6687.
- (14) Monkhorst, H. J.; Pack, J. D. Special Points for Brillouin-zone integrations. *Phys. Rev. B* **1976**, *13*, 5188.
- (15) Wu, X.; Vanderbilt, D.; Hamann, D. R. Systematic Treatment of Displacements, Strains, and Electric Fields in Density-Functional Perturbation Theory. *Phys. Rev. B: Condens. Matter Mater. Phys.* **2005**, *72*, No. 035105.
- (16) Gaillac, R.; Pullumbi, P.; Coudert, F.-X. ELATE: An Open-Source Online Application for Analysis and Visualization of Elastic Tensors. *J. Phys.: Condens. Matter* **2016**, *28*, 275201.
- (17) Herath, U.; Tavadze, P.; He, X.; Bousquet, E.; Singh, S.; Muñoz, F.; Romero, A. H. PyProcar: A Python Library for Electronic Structure Pre/Post-Processing. *Comput. Phys. Commun.* **2020**, *251*, 107080.
- (18) Togo, A.; Tanaka, I. First principles Phonon Calculations in Materials Science. *Scr. Mater.* **2015**, *108*, 1–5.
- (19) Woodley, S. M.; Battle, P. D.; Gale, J. D.; Richard A. Catlow, C. The Prediction of Inorganic Crystal Structures using a Genetic Algorithm and Energy Minimisation. *Phys. Chem. Chem. Phys.* **1999**, *1*, 2535–2542.
- (20) Lv, J.; Wang, Y.; Zhu, L.; Ma, Y. Particle-Swarm Structure Prediction on Clusters. *J. Chem. Phys.* **2012**, *137*, No. 084104.
- (21) Avendaño-Franco, G.; Romero, A. H. Firefly Algorithm for Structural Search. *J. Chem. Theory Comput.* **2016**, *12*, 3416–3428.
- (22) Brunger, A. T. Simulated Annealing in Crystallography. *Annu. Rev. Phys. Chem.* **1991**, *42*, 197–223.
- (23) Wales, D. J.; Doye, J. P. K. Global Optimization by Basin-Hopping and the Lowest Energy Structures of Lennard-Jones Clusters Containing up to 110 Atoms. *J. Phys. Chem. A* **1997**, *101*, 5111–5116.
- (24) Goedecker, S. Minima Hopping: An Efficient Search Method for the Global Minimum of the Potential Energy Surface of Complex Molecular Systems. *J. Chem. Phys.* **2004**, *120*, 9911–9917.
- (25) Amsler, M.; Goedecker, S. Crystal Structure Prediction using the Minima Hopping Method. *J. Chem. Phys.* **2010**, *133*, 224104.
- (26) Singh, S.; Zanolli, Z.; Amsler, M.; Belhadji, B.; Sofo, J. O.; Verstraete, M. J.; Romero, A. H. Low-Energy Phases of Bi Monolayer Predicted by Structure Search in Two Dimensions. *J. Phys. Chem. Lett.* **2019**, *10*, 7324–7332.
- (27) Valencia-Jaime, I.; Sarmiento-Perez, R.; Botti, S.; Marques, M. A.; Amsler, M.; Goedecker, S.; Romero, A. H. Novel Crystal Structures for Lithium–Silicon Alloy predicted by Minima Hopping Method. *J. Alloys Compd.* **2016**, *655*, 147–154.
- (28) Roy, S.; Goedecker, S.; Hellmann, V. Bell-Evans-Polanyi Principle for Molecular Dynamics Trajectories and its Implications for Global Optimization. *Phys. Rev. E* **2008**, *77*, No. 056707.
- (29) Singh, S.; Valencia-Jaime, I.; Pavlic, O.; Romero, A. H. Elastic, Mechanical, and Thermodynamic Properties of Bi-Sb Binaries: Effect of Spin-Orbit Coupling. *Phys. Rev. B: Condens. Matter Mater. Phys.* **2018**, *97*, No. 054108.
- (30) Dronskowski, R.; Bloechl, P. E. Crystal Orbital Hamilton Populations (COHP): Energy-Resolved Visualization of Chemical Bonding in Solids based on Density-Functional Calculations. *J. Phys. Chem.* **1993**, *97*, 8617–8624.
- (31) Deringer, V. L.; Tchougréeff, A. L.; Dronskowski, R. Crystal Orbital Hamilton Population (COHP) Analysis As Projected from Plane-Wave Basis Sets. *J. Phys. Chem. A* **2011**, *115*, 5461–5466.
- (32) Maintz, S.; Deringer, V. L.; Tchougréeff, A. L.; Dronskowski, R. Analytic Projection from Plane-Wave and PAW Wavefunctions and Application to Chemical-Bonding Analysis in Solids. *J. Comput. Chem.* **2013**, *34*, 2557–2567.
- (33) Maintz, S.; Esser, M.; Dronskowski, R. Efficient Rotation of Local Basis Functions Using Real Spherical Harmonics. *Acta Phys. Pol., B* **2016**, *47*, 1165.
- (34) Jain, A.; Hautier, G.; Ong, S.; Moore, C.; Fischer, C.; Persson, K.; Ceder, G. Formation Enthalpies by Mixing GGA and GGA + U Calculations. *Phys. Rev. B: Condens. Matter Mater. Phys.* **2011**, *84*, No. 045115.
- (35) Jain, A.; Ong, S. P.; Hautier, G.; Chen, W.; Richards, W. D.; Dacek, S.; Cholia, S.; Gunter, D.; Skinner, D.; Ceder, G.; et al. The Materials Project: A materials genome approach to accelerating materials innovation. *APL Mater.* **2013**, *1*, No. 011002.
- (36) Saal, J. E.; Kirklin, S.; Aykol, M.; Meredig, B.; Wolverton, C. Materials Design and Discovery with High-Throughput Density Functional Theory: The Open Quantum Materials Database (OQMD). *JOM* **2013**, *65*, 1501–1509.
- (37) Singh, S.; Valencia-Jaime, I.; Pavlic, O.; Romero, A. H. Elastic, Mechanical, and Thermodynamic Properties of Bi-Sb Binaries: Effect of Spin-Orbit Coupling. *Phys. Rev. B: Condens. Matter Mater. Phys.* **2018**, *97*, No. 054108.
- (38) Pugh, S. XCII. Relations between the Elastic Moduli and the Plastic Properties of Polycrystalline Pure Metals. *London, Edinburgh, and Dublin Philos. Mag. (1798–1977)* **1954**, *45*, 823–843.
- (39) Ranganathan, S. I.; Ostoja-Starzewski, M. Universal Elastic Anisotropy Index. *Phys. Rev. Lett.* **2008**, *101*, No. 055504.
- (40) Kube, C. M. Elastic Anisotropy of Crystals. *AIP Adv.* **2016**, *6*, No. 095209.
- (41) Serrano, J.; Kremer, R.; Cardona, M.; Siegle, G.; Romero, A.; Lauck, R. Heat Capacity of ZnO: Isotope Effects. *Phys. Rev. B: Condens. Matter Mater. Phys.* **2006**, *73*, No. 094303.
- (42) Chkhartishvili, L. Isotopic Effects of Boron. *Trends Inorg. Chem.* **2009**, *11*, 105–167.
- (43) Auerbach, N. Nuclear Structure of the Nickel Isotopes. *Phys. Rev.* **1967**, *163*, 1203.
- (44) Yntema, J.; Satchler, G. (d, He 3) Reaction on Ca 40 and the Titanium Isotopes. *Phys. Rev.* **1964**, *134*, B976.
- (45) Sanati, M.; Estreicher, S.; Cardona, M. Isotopic Dependence of the Heat Capacity of c-C, Si, and Ge: an ab Initio Calculation. *Solid State Commun.* **2004**, *131*, 229–233.
- (46) Yurko, G. A.; Barton, J. W.; Parr, J. G. The Crystal Structure of Ti₂Ni. *Acta Crystallogr.* **1959**, *12*, 909–911.
- (47) Toprek, D.; Belosevic-Cavor, J.; Koteski, V. Ab Initio Studies of the Structural, Elastic, Electronic and Thermal Properties of NiTi₂Intermetallic. *J. Phys. Chem. Solids* **2015**, *85*, 197–205.
- (48) Momma, K.; Izumi, F. VESTA: A Three-Dimensional Visualization System for Electronic and Structural Analysis. *J. Appl. Crystallogr.* **2008**, *41*, 653–658.
- (49) Dagdelen, J.; Montoya, J.; de Jong, M.; Persson, K. Computational Prediction of New Auxetic Materials. *Nat. Commun.* **2017**, *8*, 323.
- (50) Gaillac, R.; Pullumbi, P.; Coudert, F.-X. ELATE: An Open-Source Online Application for Analysis and Visualization of Elastic Tensors. *J. Phys.: Condens. Matter* **2016**, *28*, 275201.
- (51) Cairns, A. B.; Catafesta, J.; Levelut, C.; Rouquette, J.; van der Lee, A.; Peters, L.; Thompson, A. L.; Dmitriev, V.; Haines, J.; Goodwin, A. L. Giant Negative Linear Compressibility in Zinc-di-cyanoaurate. *Nat. Mater.* **2013**, *12*, 212–216.
- (52) Cairns, A. B.; Goodwin, A. L. Negative Linear Compressibility. *Phys. Chem. Chem. Phys.* **2015**, *17*, 20449–20465.
- (53) Guo, Y.; Goddard, W. A. Is Carbon Nitride Harder than Diamond? No, but its Girth Increases when Stretched (Negative Poisson Ratio). *Chem. Phys. Lett.* **1995**, *237*, 72–76.

(54) Kimizuka, H.; Kaburaki, H.; Kogure, Y. Mechanism for Negative Poisson Ratios over the α - β Transition of Cristobalite, SiO₂: A Molecular-Dynamics Study. *Phys. Rev. Lett.* **2000**, *84*, 5548–5551.

(55) Baughman, R. H.; Stafström, S.; Cui, C.; Dantas, S. O. Materials with Negative Compressibilities in One or More Dimensions. *Science* **1998**, *279*, 1522–1524.